Al-Fe-Ce alloy processed by laser powder bed fusion: microstructure and mechanical characterization

Materials Science & Engineering A 947 (2025) 149252

Contents lists available at ScienceDirect

Materials Science & Engineering A

journal homepage: www.elsevier.com/locate/msea

Al-Fe-Ce alloy processed by laser powder bed fusion: microstructure and mechanical characterization

Nicolò Arcieri [a,*], Silvia Marola [b], Marco Actis Grande [c,d], Diego Manfredi [a,d]

[a] Department of Applied Science and Technology (DISAT), Politecnico di Torino, Corso Duca degli Abruzzi 24, 10129, Turin, Italy
[b] Department of Mechanical Engineering, Politecnico di Milano, Via G. La Masa 1, 20156, Milan, Italy
[c] Department of Applied Science and Technology (DISAT), Politecnico di Torino, Viale T. Michel 5, 15121, Alessandria, Italy
[d] Center of Integrated Additive Manufacturing (IAM), Politecnico di Torino, Corso Castelfidardo, 51, 10138, Turin, Italy

ARTICLE INFO

Keywords:
Al alloys
Additive manufacturing
Laser powder bed fusion
Intermetallic phases
High strength

ABSTRACT

Laser powder bed fusion for metals (PBF-LB/M) was employed to consolidate an Al-8 %Fe-4 %Ce (wt %) alloy originally developed for conventional powder metallurgy processes. This study focuses on the characterization of the as-built microstructure and its mechanical properties at room temperature. Although its high tendency to solid state cracking, crack-free samples with a density of 99.5 % were successfully produced. The as-built microstructure consists of columnar grains, with melt pools containing a high-volume fraction of reinforcing intermetallic phases dispersed in the Al matrix. High-resolution backscattered electron imaging revealed that the melt pool boundary region consists of a cellular structure enriched in Ce and Fe, within which dispersoids are distributed. Conversely, the melt pool center exhibits an ultrafine cellular microstructure. Multiple intermetallic phases were identified using X-ray diffraction, including: the stable phases $Al_{13}Fe_4$ and $Al_{11}Ce_3$ and the metastable Al_6Fe. Thermal analyses show the exceptional thermal stability of the alloy at temperatures up to 580 °C. Finally, the alloy exhibits excellent mechanical properties, with an average tensile strength of 530 MPa and an average microhardness of 201 $HV_{0.5}$. The combination of thermal stability and high strength makes this alloy attractive for applications beyond 200 °C, which can be attributed to the low diffusion alloying elements Fe and Ce.

1. Introduction

The term additive manufacturing (AM) refers to all those fabrication processes in which the object is created in a layer wise way starting from a computer aided drawing (CAD) [1]. This approach allows to produce complex shape objects otherwise impossible to create with traditional manufacturing methods such as casting or machining [1,2]. Among the AM technologies, laser powder bed fusion for metals (PBF-LB/M) is by far the most widely used process for the industrial fabrication of metallic components [3]. The high cooling rates (10^3–10^7 K/s) achieved during PBF-LB/M create uniquely refined microstructures enhancing the mechanical properties of the material [2].

Aluminum alloys are broadly used across several industrial fields due to their attractive properties, including lightweight, good mechanical properties and excellent corrosion resistance [2]. Typical alloys commonly processed by PBF-LB/M are those belonging to the family of casting Al-Si alloys [2,4,5]. The benchmark for PBF-LB/Med Al alloys is AlSi10Mg, as it can be easily processed by PBF-LB/M, due to its near eutectic composition [2,4]. However, even though the refined microstructure derived from the rapid cooling gives better mechanical properties than its casting counterpart, this alloy could not be suitable for structural applications in demanding industrial sectors like the aerospace field. Wrought alloys of 2xxx series (Al-Cu) and 7xxx (Al-Zn) are commonly used in applications requiring high strength [2]. Nevertheless, their fabrication by PBF-LB/M is challenging due to the high susceptibility to hot tearing, often making necessary to add nucleating agents to improve processability [2,4–6]. Therefore, in the last few years, enormous efforts have been directed to develop high strength Al alloys able to fully take advantage of the rapid solidification derived from the PBF-LB/M process. As a result, Airbus designed a high-strength Al alloy based on the Al-Mg-Sc-Zr system, commercially known as Scalmalloy© [7,8]. The presence of Sc and Zr improves the printability of the alloy and, in addition, enhances its mechanical properties through the precipitation of $L1_2$-Al_3(Sc,Zr) intermetallics [8]. However, Sc is a

* Corresponding author.
E-mail address: nicolo.arcieri@polito.it (N. Arcieri).

https://doi.org/10.1016/j.msea.2025.149252
Received 29 July 2025; Received in revised form 6 October 2025; Accepted 9 October 2025
Available online 10 October 2025

costly and rare alloying element, thus limiting the use of the alloy only in high-end applications [5]. Other high-strength Al alloys which gained attention for PBF-LB/M are those based on the Al-Ce system [5,6,9–11]. Al-Ce alloys are attractive since they offer various advantages over traditional compositions. Besides providing a narrow freezing point that enhances alloy processability [11], the Al-$Al_{11}Ce_3$ eutectic (formed at 10–12 wt% Ce) [9,12] possesses high thermal stability, with a melting point close to that of pure Al [12]. Ce also exhibits a low diffusion coefficient in the α-Al matrix at high temperatures, which improves the coarsening resistance of the Ce-rich intermetallic phases [9,13]. From an economic and environmental perspective, Ce is considered a byproduct of the refinement of higher value rare earth elements (REEs) and is often discarded [12,14,15]. Expanding its use as alloying element in Al alloys would create a new market for this REE, enhancing the overall economic sustainability of REE production [16]. In addition to Al-Ce based alloys, Al-Fe alloys are becoming more and more investigated as high-strength Al alloys for PBF-LB/M [17–26]. Fe is the most common impurity found in Al alloys. It tends to negatively affect the mechanical performance of casting Al-Si alloys due to the formation of coarse needle-like intermetallics such as $Al_{13}Fe_4$ and β-AlFeSi due to its low solid solubility in the α-Al matrix [26–28]. A minimum amount of Fe is always present in Al alloys due to its natural occurrence in the bauxite ore [15]. Additionally, the average Fe content tends to rise when the aluminum comes from scrap recycling. Therefore, considering the growing trend of recycling Al, the average Fe content in Al alloys is expected to steadily increase in the next few years [28]. As a result, keeping Fe content low will be increasingly challenging. Several studies [17–26] investigated the effect of processing Al-Fe alloys by means of PBF-LB/M, evidencing that the resulting microstructure is characterized by refined Fe-rich intermetallics granting attractive mechanical properties to the material [17–26]. Al-Fe alloys have also exhibited good thermal stability. In fact, various alloys for PBF-LB/M based on Al-Fe system demonstrated excellent mechanical properties up to 300 °C and good mechanical behavior even up to 500 °C, making them interesting for structural applications in harsh environments [19,25]. Finally, using a high amount of Fe as the main alloying element would lower the material costs, given its abundance and affordability.

Heat resistant and high strength Al-Fe-Ce alloys were originally developed in the 1980's as substitutes for titanium alloys in structural applications up to 350 °C [29–33]. The industrial production of alloys with a high content of Fe and Ce was made possible by a combination of rapid solidification (gas atomization) and powder metallurgy (PM) processes. Among these alloys, AA 8019 or Al-8Fe-4Ce (all the compositions are in wt%, unless otherwise stated) was one of the most extendedly characterized. However, its applications have been limited so far due to its expensive and time-consuming fabrication process. In fact, the alloy undergoes various production steps, including gas atomization, cold pressing, vacuum hot pressing and finally hot working [31]. In addition, only simple geometries can be created, as complex shape components would require additional machining steps. Therefore, PBF-LB/M can be seen as an interesting alternative fabrication route for Al-8Fe-4Ce. Few studies investigated the processability of the Al-Fe-Ce system by PBF-LB/M in the last few years. Chernyshikhin et al. [34] fabricated an Al alloy containing 2.28 wt% Ce and 1.28 wt% Fe as main alloying elements. They were able to successfully produce samples with a residual porosity of 0.2 %. The studied alloy showed excellent thermal stability at temperatures up to 300 °C, but with a relatively low room temperature tensile strength of 250 MPa. Park et al. [35] demonstrated that laser remelted Al-10Ce-1Fe shows a hardness double compared to the cast alloy, suggesting its potential processability by PBF-LB/M.

To the best of the authors' knowledge, no attention has been paid so far to Al-8Fe-4Ce processed by PBF-LB/M, despite the alloy has already shown attractive properties when processed by traditional PM processes. This is likely due to the fact that most of the efforts have been focused on adapting cast and wrought Al alloys to the PBF-LB/M process, while only few studies [5,36,37] have explored Al alloys derived from traditional PM. However, the latter are the most attractive, as they are already designed to benefit from rapid solidification. Therefore, this work aims to evaluate the feasibility of processing Al-8Fe-4Ce, hereafter designed as Al-Fe-Ce, by means of PBF-LB/M. Although this proved particularly challenging due to the inherently high-volume fraction of intermetallic phases, optimal processing parameters were identified to obtain crack-free, dense samples. These samples were first analyzed by X-ray Diffraction (XRD) to identify the phases present both in the feedstock material as well as those formed during the PBF-LB/M process, and by Differential Scanning Calorimetry (DSC) to evaluate the thermal stability of the alloy. Thermodynamic simulations were also performed using Thermo-Calc® software. The microstructure was investigated by electron microscopy with the support of Electron Back Scattered Diffraction (EBSD) analysis, to evaluate the effects of the rapid solidification on this alloy. The experimental observations were compared to the predictions based on equilibrium and Scheil-Gulliver solidification curves. Microhardness, nanohardness and tensile properties at room temperature were evaluated to have a complete picture of the mechanical properties of this alloy after being processed by PBF-LB/M. Post-mortem analyses were carried out on surface fracture of tested tensile specimens to study the failure mechanisms.

2. Materials and methods

2.1. Powder feedstock and sample production

The Al-Fe-Ce gas atomized powder, with chemical composition reported in Table 1, was purchased from Valimet (Stockton, United States). Powder morphology was investigated using a field emission scanning electron microscope (FESEM) Zeiss Supra TM 40. The particle size distribution (PSD) of the gas atomized powders was determined using a laser granulometry Mastersizer 3000 analyser.

PBF-LB/M samples were manufactured using a Print Sharp 250 system (Prima Adddditive, Italy). The system is equipped with a 500 W Yb: YAG IR fiber laser, with a spot size of 0.1 mm, operating with an Ar shielding atmosphere. To find a proper processability window, 10 ×10 × 10 mm^3 cubic samples were printed varying the laser power in the range 300–400 W with a step of 50 W and the scanning speed in the range 900–1300 mm/s with a step of 100 mm/s, while keeping the other parameters fixed. A cross-ply 0°–90° strategy was used as scanning strategy.

After printing, samples were removed from the building platform using a wire electric discharge machine (W-EDM) Baoma BMW-3000. Then, they were observed under a stereomicroscope Leica EZ4 W to check the presence of eventual microcracks. Relative density of crack-free samples was measured by means of Archimede's method. A theoretical density of 2.95 g/cm^3 was used as reference. Once the optimal process parameters were found, specimens for microstructural analysis and mechanical testing in the form of parallelepipeds of 105× 4 × 15 mm^3 were built. These were placed on the building platform with the side of 15 mm parallel to the building direction (BD).

2.2. Microstructural investigation

Samples were cut parallel to the building direction and polished following the standard metallographic procedure for the microstructural analysis. XRD patterns were acquired by means of a Malvern Panalytical Empyrean X-ray diffractometer in Bragg-Brentano configuration, using the K_α emission line of a Cu filament (λ_{Cu} = 1.5406 Å). Data were

Table 1
Chemical composition of the powder feedstock measured by ICP-OES. The values are given in wt%.

Al	Fe	Ce	Si	Mn	Ti	Zn	Others
Bal.	7.75	4.31	0.12	0.04	0.01	0.01	<0.15

collected in the range 15°–140° with a step size of 0.013° and a time per step equal to 30 s. Phase identification was carried out using the Panalytical HighScore Plus software. The microstructure was investigated using a FESEM (Zeiss Sigma 500) equipped with an Oxford Instruments Ultim Max energy dispersive X-ray spectroscopy (EDS) detector and an Oxford instrument C-Nano electron EBSD detector. EBSD analyses were performed using a step size of 0.15 μm. A few samples were etched with a 0.5 % HF solution for 5 s, in order to highlight the microstructural features. Thermal analyses were performed using a Themys One DSC by Setaram. Two identical heating and cooling cycles were carried out consecutively in order to study the material both in the as-built condition and in the near equilibrium state. Measurements were performed under a 20 ml/min argon flux in a temperature range spanning from 25 °C to 950 °C at a heating rate of 10 °C/min. The heat flux was equilibrated both at low and high temperature for each cycle. Thermodynamic simulations were performed using Thermo-Calc® software (version 2023a, database TCAL 8: Al-Alloys v8.2). Both equilibrium and Scheil-Gulliver solidification curves under non-equilibrium condition were calculated, and the results obtained were compared with the experimental observations.

2.3. Mechanical testing

Firstly, an HNVS-1000DX hardness tester was employed to perform Vickers microhardness measurements. A series of 15 microhardness indentations per sample along the build direction (or z axis) were obtained by applying a static load of 0.5 kg for a dwell time of 10 s. Then nanomechanical characterization was conducted using a Bruker/Hysitron Triboindenter TI 950. A Berkovich tip was chosen as indenter. A matrix of 300 nanoindentations was performed. The maximum load was fixed at 2.5 mN, the loading/unloading velocity was 100 μN/s, the holding time was 5 s and the spacing between nanoindentations was set at 7.5 μm. The results were analyzed applying the Oliver-Pharr method [38]. Nanoindentations were also observed using a FESEM Zeiss Supra 40.

Tensile samples were obtained by machining the parallelepiped samples into dog-bone shaped specimens with a rectangular cross-section, following the ASTM E8/E8M standard. The specimens had a gauge length of 32 mm, a width of 6 mm and a thickness of 4 mm. The loading direction was chosen perpendicular to the build direction. Tensile tests were carried out at a strain rate of $8x10^{-3}$ s^{-1} using a universal testing machine Zwick Roell BT1-FR1000 equipped with an extensometer. At least three tests were performed to ensure data reliability. The fractured surfaces were investigated by FESEM analysis.

3. Results

3.1. Alloy processability

Fig. 1a shows the spherical shape of the powder with the negligible presence of small satellites. Fig. 1b reports the PSD of the feedstock, evidencing D_{10}, D_{50} and D_{90} values respectively of 23 μm, of 40 μm and of 66 μm. These percentile values indicate that 10 %, 50 % and 90 % of the particles are equal to or smaller than the corresponding size. Such values are in agreement with the common PBF-LB/M ranges and suggest adopting a layer thickness of 30 μm.

As expected, Al-Fe-Ce alloy exhibited a tendency to solid-state cracking. Although the PBF-LB/M process was closely monitored and no apparent defects were observed during the fabrication, solid-state cracks were found in several samples while exploring the processability window. Fig. 2a and b displays unoptimized samples with different degrees of solid-state cracking. No hot cracks were observed in any sample. Despite the solid-state cracking issue, crack-free specimens were finally printed with a relative density of 99.5 % (see Fig. 2c) using the process parameters reported in Table 2.

3.2. XRD

Representative XRD patterns are reported in Fig. 3a for the powder as received and for samples in as-built condition. The angular ranges between 15° and 37° and between 38° and 50° are magnified to provide a clearer view of the diffraction peaks in these two intervals (see Fig. 3b and c). PBF-LB/M sample pattern showed less intense and broader signals than the powder. This is due to the higher cooling rate achieved during the PBF-LB/M process in comparison to the solidification rate of gas atomization [39], which leads to a reduction in the crystallite size. Distinctive peaks of the α-Al were detected in both patterns, as expected. The (200) peak in the PBF-LB/M pattern exhibited a higher intensity than that reported in the reference pattern for Al (PDF #00-004-0787). This suggests a certain degree of texture in the material, which is likely due to the scanning strategy employed during the fabrication process. The remaining peaks were attributed to $Al_{11}Ce_3$, Al_6Fe, and $Al_{13}Fe_4$ phases. However, a few low intensity peaks, especially in the powder pattern, remain unidentified because no satisfactory match was found in the available database. It is worth noticing that, unlike what reported in literature for alloys based on Al-Ce-Fe system [15,32,34,35] where the equilibrium $Al_{10}Fe_2Ce$ and the metastable Al_8Fe_2Ce phases are often observed, they do not appear to be present in this case. In fact, no match was found between the unidentified peaks and the ICSD patterns of these two phases (ICSD pattern #188958 and #107229, respectively).

3.3. Thermal analyses

DSC analyses were performed to investigate the thermal stability of the alloy when increasing the temperature given its potential applications at service temperatures beyond 200 °C. Fig. 4 illustrates the DSC curves for the Al-Fe-Ce alloy in the as-built condition. Two cycles were carried out to study the alloy in the as-built and near equilibrium conditions. The as-built alloy showed a small exothermic peak with an onset

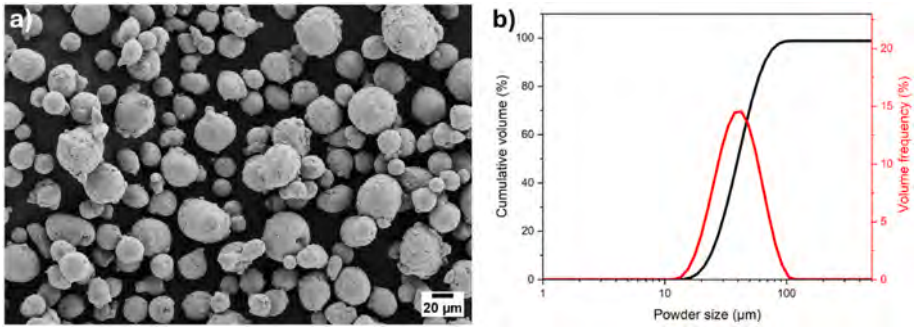

Fig. 1. Al-Fe-Ce alloy gas atomized powder. (a) Secondary electron FESEM image showing the powder morphology. (b) Volume particle size distribution (red color) and cumulative particle size distribution (black color) of the feedstock. (For interpretation of the references to color in this figure legend, the reader is referred to the Web version of this article.)

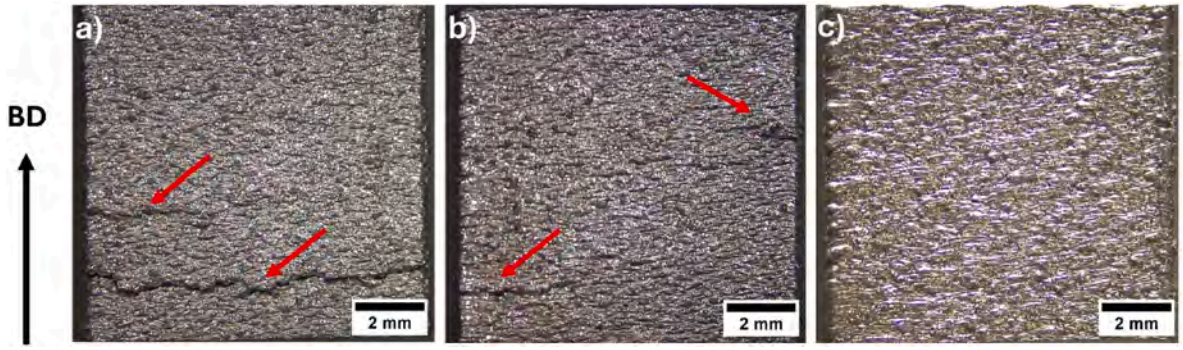

Fig. 2. Cubic samples of Al-Fe-Ce alloy. (a) Extensively cracked sample, (b) partially cracked sample and (c) crack-free sample. Solid-state cracks are marked by red arrows. (For interpretation of the references to color in this figure legend, the reader is referred to the Web version of this article.)

Table 2
Process parameters used for Al-Fe-Ce alloy by PBF-LB/M to obtain crack free dense samples.

Parameters	Values
Laser power (P)	400 W
Scanning speed (v)	1200 mm/s
Hatch distance (h)	0.16 mm
Layer thickness (t)	0.03 mm
Scanning Strategy	0°–90°
Platform temperature	150 °C

temperature of approximately 580 °C during heating. This peak is present only in the first cycle, as it was not detected during the second heating cycle. This was followed by a strong endothermic signal with an onset at 647 °C. In the second heating ramp, the strong endothermic peak shifted slightly to a lower onset temperature (639 °C). In addition, the peak shape changed in the second heating cycle. It can be observed that the cooling ramps are almost perfectly overlapping, as both describe solidification near the equilibrium condition. Therefore, they are described as one. During cooling, an exothermic event occurred at the onset temperature of 871 °C. Then, an intense exothermic peak was recorded at 645 °C. The shape of this peak suggests the overlapping of various phenomena within a narrow temperature range.

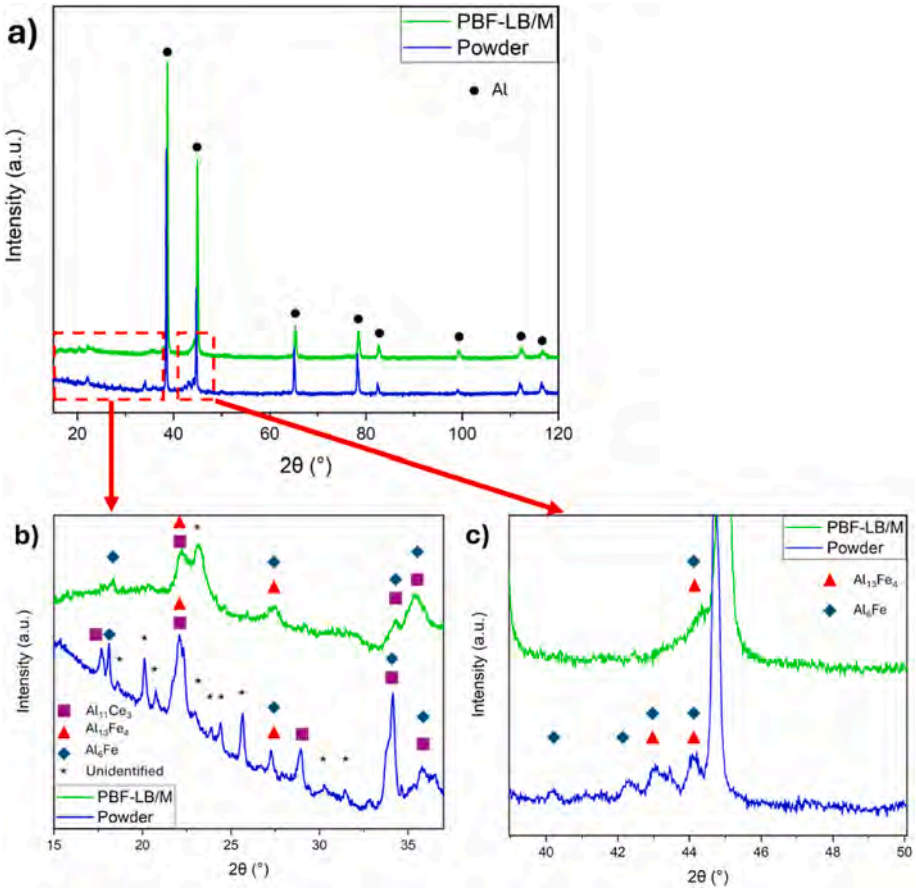

Fig. 3. (a) XRD patterns for Al-Fe-Ce alloy powder (blue) and Al-Fe-Ce alloy processed by PBF-LB/M (green). (b) Details for the 15°–37° range. (c) Details for the 38°–50° range. (For interpretation of the references to color in this figure legend, the reader is referred to the Web version of this article.)

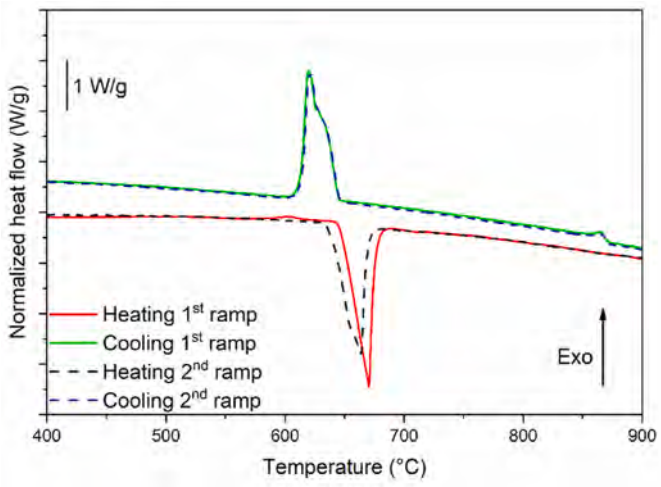

Fig. 4. DSC scans for Al-Fe-Ce alloy performed at 10 °C/min.

3.4. Microstructure

Employing a FESEM, InLens and Secondary electron (SE) imaging were performed on etched samples to gain insights on the as-built microstructure. Fig. 5a shows how the etching reveals the melt pool morphology and arrangement, with alternating elongated and rounded melt pools. This pattern is typical for a material processed using a 0°–90° strategy. In addition, Fig. 5a displays no significant process defects, with the exceptions of a gas pore, as indicated by the red arrow. Observing the overlapping of several melt pool boundaries (MPBs) in Fig. 5b, it becomes evident that the etching process effectively revealed a high-volume fraction of intermetallic phases. This is particularly clear in the magnified view shown in Fig. 5c, where the intermetallics display a notably regular and distinctive shape. In addition, the dispersoids are surrounded by a coarse cellular/dendritic microstructure, as visible in the upper limit of the MPB (see Fig. 5d) due to the increase in cooling rate towards the melt pool center. This can easily result by the steep thermal gradient caused by the inherently localized nature of the fabrication process.

EDS through FESEM was employed to investigate the inhomogeneous phase distribution in the MPB region as shown in Fig. 6. The analysis provides valuable insights into the composition of the intermetallic phases. The relatively coarse intermetallics are identified as Fe-rich dispersoids, as illustrated by Fig. 6. On the other hand, Ce-rich intermetallics cannot be clearly distinguished, as Ce seems to be evenly distributed throughout the Al matrix. In addition, Fe is not only concentrated in the dispersoids but also in the Al matrix. This might suggest that the cellular microstructure observed in Fig. 5d can be enriched in both Fe and Ce.

Unetched samples were studied using high-resolution backscattered electron (HRBSE) mode (see Fig. 7a–c) to take advantage of the large difference in atomic number between Al and the main alloying elements (i.e., Fe and Ce). Fig. 7a displays a representative region where multiple MPBs, outlined by white dotted lines, overlap. Here, the microstructure shifts from a very fine cellular structure to a coarse cellular/dendritic microstructure moving from the center of the melt pool towards the MPB. A closer examination of the MPB region (Fig. 7b–d) confirms that the network is enriched in both Fe and Ce, within which multiple intermetallic phases are dispersed. The brightest intermetallics are the ones enriched in Ce, while the others are rich in Fe. Moving towards the melt pool center (Fig. 7e), the microstructure becomes extremely refined. Here, the dispersoids are likely to have a nanometer size, confirming the beneficial effect of the rapid cooling on their microstructure refinement.

EBSD analyses were performed on the as-built Al-Fe-Ce alloy. The corresponding inverse pole figure (IPF) map is shown in Fig. 8a. The IPF map reveals that the microstructure consists mainly of large columnar grains that have grown epitaxially across the MPB following the direction of maximum heat transfer. There are also local unidentified areas in the IPF map (black areas), probably due to the large amount of fine intermetallic precipitates. On the other hand, the kernel average misorientation (KAM) map for Al-Fe-Ce alloy, shown in Fig. 8b, highlights a high level of local strain mainly concentrated along the MPB regions and the low angle grain boundaries. Indeed, KAM map represents the local misorientation caused by plastic deformation in the material [40], providing information on the residual stresses within the

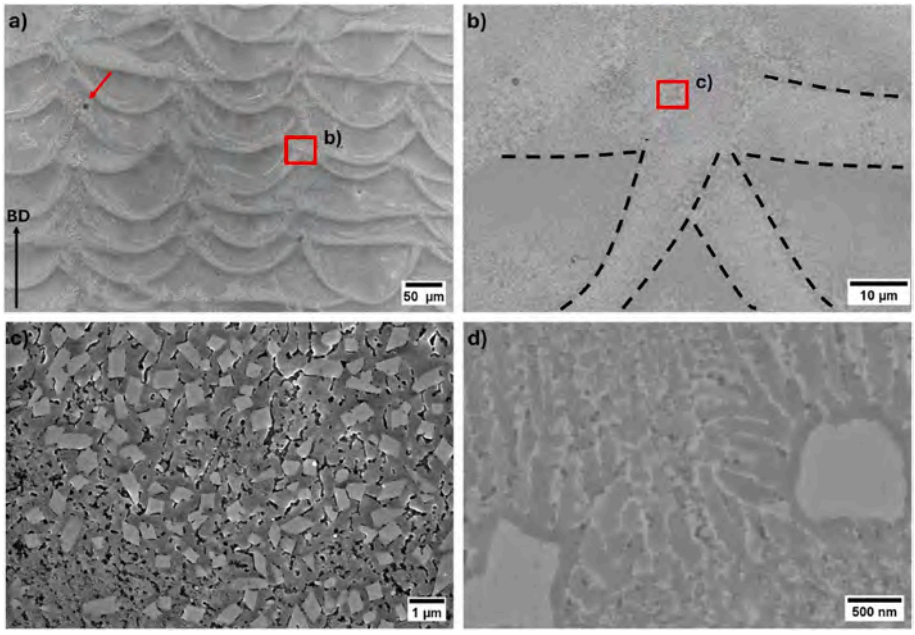

Fig. 5. Micrographs of the cross-section after etching. (a) Overview of the microstructure in InLens mode. (b) InLens image of the overlap of multiple melt pool boundaries (MPBs), with the edges of MPBs highlighted by black dotted lines. (c) InLens image within MPB region, showing the large volume fraction of intermetallic phases in this region. (d) SE image of the upper MPB region, illustrating the cellular/dendritic microstructure.

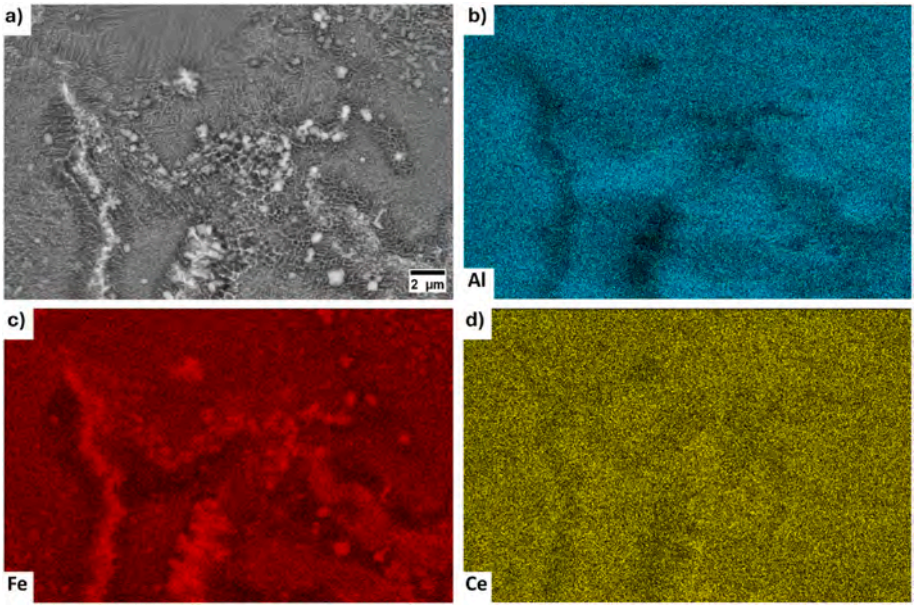

Fig. 6. (a) FESEM Micrograph of the analyzed area using EDS. EDS data for (b) Al, (c) Fe and (d) Ce distribution.

material induced by the heating and cooling cycles associated with the PBF-LB/M process. Finally, it can be seen a strong ⟨001⟩ texture along the BD, as shown by the high intensity in ⟨001⟩ in Fig. 8c.

3.5. Mechanical behavior

Mechanical properties for as-built Al-Fe-Ce alloy were first assessed by measuring its microhardness along the build direction. The alloy exhibits an outstanding microhardness of 201 ± 13 $HV_{0.5}$. This value is far superior to those reported for Al-Si alloys processed by PBF-LB/M (see Table 3) [41,42] and similar to Al-15Fe (196 $HV_{0.2}$), which was designed as a high strength Al alloy for harsh environments [19].

Nanoindentation was performed considering an area through different melt pools, with the aim of gaining insights on the variation in nanohardness between different microstructural features. Fig. 9a illustrates a portion of the nanoindentation matrix performed. The average nanohardness recorded for Al-Fe-Ce alloy is presented in Table 3 along with that of other PBF-LB/Med Al alloys measured under the same loading conditions [42]. Al-Fe-Ce shows a higher average nanohardness compared to AlSi10Mg and AlSi10Mg + 4 % Cu. The alloy exhibits a peak nanohardness of 3.6 GPa in the intermetallic-rich regions. In addition, despite the large amount of intermetallics, the measurement is characterized by a lower standard deviation than the mechanical alloyed AlSi10Mg + 4 % Cu, supporting the thesis that the majority of the intermetallics are very fine and homogeneously distributed (see Fig. 9b).

Fig. 10a illustrates the tensile properties of as-built Al-Fe-Ce alloy at room temperature. The alloy exhibits excellent yield strength (YS, measured using the 0.2 % method) and ultimate tensile strength (UTS) mean values of 358 ± 1.8 MPa and 530 ± 1.6 MPa, respectively. The mean value for elongation at failure (El) is 2.63 ± 0.04 % for as-built Al-Fe-Ce alloy. When the properties are compared to those of traditional PM counterpart, they fall within the upper range of values reported in the literature (YS = 326 ÷ 486 MPa, UTS = 434 ÷ 560 MPa, and El = 2.1 ÷ 3 %) [30,33,43], especially regarding UTS and El. This great variability in mechanical properties for PM Al-Fe-Ce is likely attributed to the different hot forming processes to which the alloy can be subjected after the consolidation. Examples of the fracture surface of tensile samples are shown in Fig. 10b–d. Despite the limited elongation at failure, the fracture surfaces showed a certain degree of ductility, as evidence by the presence of dimples. Moreover, platelet-like intermetallics were observed within the dimples, as pointed out in Fig. 10d.

4. Discussion

4.1. Thermodynamic simulation and hot tearing resistance

As illustrated in the Results section, crack-free, dense Al-Fe-Ce samples were successfully printed and mechanically tested. As expected, solid-state cracking was the main defect observed during the definition of process window parameters. In fact, this kind of defect can occur when Al alloys forming a high percentage of intermetallics are processed by PBF-LB/M. This phenomenon was also observed in other high strength aluminum alloys with a high-volume fraction of intemertallic phases, such as Al-Fe-V-Si [36,37], Al-Fe-Mo-Si-Zr [22] and Al-Ce-Ni-Mn [9], when processed by PBF-LB/M. In solid-state cracking, cracks tend to be perpendicular to the building direction and propagate along the MPBs, which are the intermetallic-rich regions. The main reason for that can be related to residual stresses generated during the process combined with the large lattice mismatch between the matrix and the intermetallic phases, similar to what has been observed in Ni superalloys [44,45]. A few strategies [9,36] have been suggested in order to mitigate solid-state cracking in Al alloys. A stress-relief treatment at high temperature (up to 450 °C) before removing the samples from the platform can relieve most of the residual tension [9]. However, the drawback of this approach is the destruction of the refined microstructure produced during the PBF-LB/M fabrication. Sun et al. [36] observed that reducing heat input by increasing the scanning speed and the hatch distance, along with using a preheated platform, effectively reduced solid-state cracking sensitivity. In addition, the use of a 67° strategy can also help in reducing residual stress in the material during consolidation [46]. Finally, using a top-hat laser profile might reduce the solid-state cracking issue [37]. In this work, the processability window was identified in the region of high scanning speeds (1200 mm/s) combined with a relatively large hatch distance (0.16 mm) and a preheated platform (150 °C) supporting the hypothesis that Sun's approach can be effective in reducing the solid-state cracking while maintaining the refined microstructure.

While solid-state cracks were observed, no hot cracks were found in Al-Fe-Ce samples. The absence of hot tearing was expected due to the short solidification range of this alloy, as shown by its Scheil-Gulliver

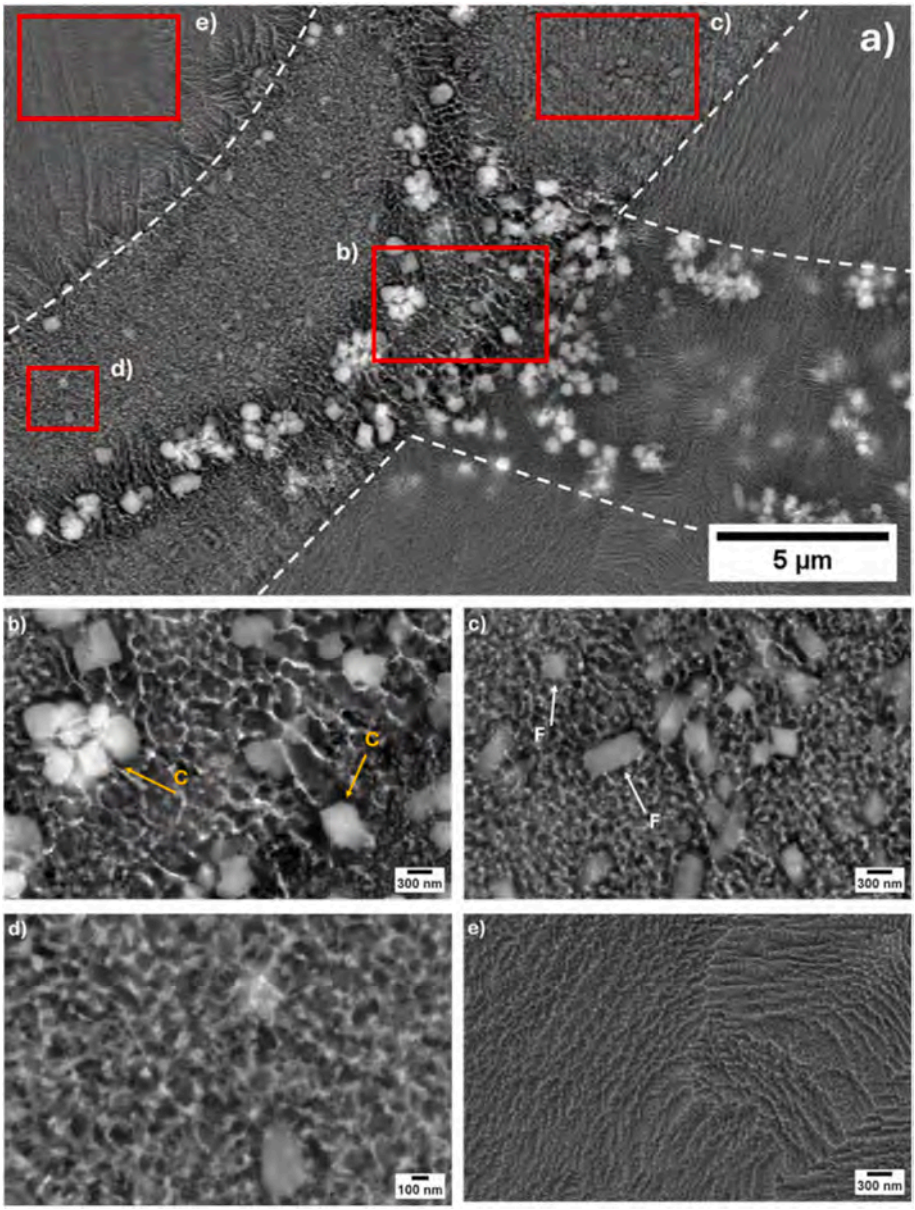

Fig. 7. High resolution BSE imagining of as-built Al-Fe-Ce alloy. (a) Intersection of multiple MPBs. (b–d) Enlarge area showing Ce-rich (marked as "C") and Fe-rich (marked as "F") intermetallic phases. (e) Details of the melt pool center region, showing an ultrafine microstructure.

solidification curve (see Fig. 11a). Hot cracking, also known as hot tearing, tends to occur due to the hindered shrinkage inside the mushy zone during the solidification process [47]. The mushy zone in Al alloys often consists mainly of columnar grains between which there is the liquid. During the final solidification stages, when the solid fraction (f_s) approaches unity, the tensile strains can no longer be accommodated by the rearrangement of the grains due to the lack of liquid, thus generating a crack along the grains. Cracks generally form parallel to the build direction in additive manufactured (AMed) alloys. Kou [47] proposed a criterion in order to determine the susceptibility of Al alloys to hot cracking. It was originally developed for casting and welding Al alloys but has also been successfully applied to AMed Al alloys [11,48]. Kou's criterion takes into account the solidification curve in the final stage of solidification, as $f_s \rightarrow 1$, and expresses the index for crack susceptibility as [47]:

$$\max \left| \frac{dT}{df_s^{1/2}} \right| f_s \rightarrow 1 \quad (1)$$

where T is the temperature. Then, the index for crack susceptibility corresponds to the maximum value of the curve slope (dT/df_s) when $f_s \rightarrow 1$.

For Al-Fe-Ce alloy, it is obvious that the value of dT/df_s is near to zero when $f_s \rightarrow 1$. Fig. 11b compares the value of crack susceptibility index for the Al-Fe-Ce alloy to those reported for other common Al alloys in literature [11,49]. The higher the value, the more likely the hot tearing is. The highest values of the index belong to alloys with a well-known tendency to hot tearing (i.e. AA6061, AA7075, AA2024). On the other hand, the Al-Fe-Ce alloy shows the lowest value, confirming once more what was observed experimentally. Its value is even lower than that of AlSi10Mg, which, owing to its well-known high hot tearing resistance, is the main Al alloy employed in PBF-LB/M.

Although the thermodynamic simulation was able to predict the hot tearing resistance of Al-Fe-Ce system, it appears to be inadequate in accurately describing phase formation in the alloy during solidification. In fact, neither the Scheil-Gulliver model nor the equilibrium model (see Fig. 11c) were able to fully predict the phases observed in the XRD

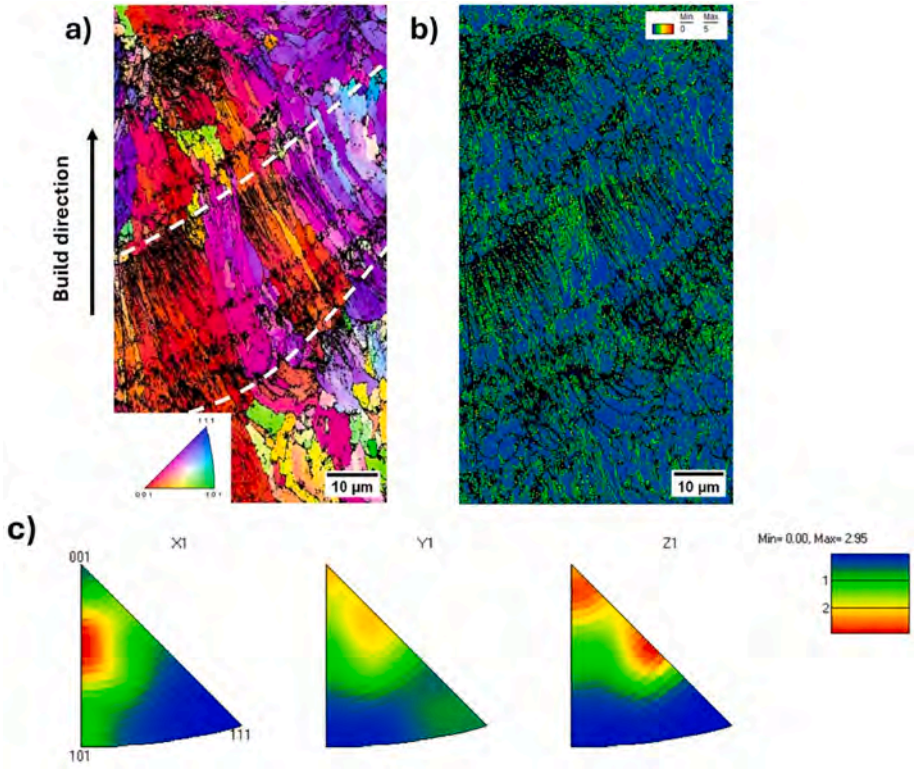

Fig. 8. EBSD analysis of Al-Fe-Ce alloy. (a) Inverse pole figure (IPF) map shows large columnar grains in the as built condition. (b) Corresponding kernel average misorientation (KAM) map. (c) Inverse pole figures.

Table 3
Microhardness and nanohardness for the Al-Fe-Ce alloy and PBF-LB/Med Al-Si alloys.

	Al-Fe-Ce	AlSi10Mg [42]	AlSi10Mg + 4 % Cu [42]
Microhardness	201 ± 13 $HV_{0.5}$	137 ± 13 $HV_{0.3}$	152 ± 5 $HV_{0.3}$
Nanohardness (GPa)	2.6 ± 0.4	2.0 ± 0.2	2.4 ± 0.8

pattern. The former anticipated the formation of α-Al, $Al_{11}Ce_3$ and $Al_{10}Fe_2Ce$ phase while the latter the formation of α-Al, $Al_{13}Fe_4$ and $Al_{10}Fe_2Ce$ phases. However, as illustrated in section 3.2, peaks referring to α-Al, $Al_{13}Fe_4$ and $Al_{11}Ce_3$ were identified along with those of metastable Al_6Fe. Evidence of the equilibrium $Al_{10}Fe_2Ce$ phase was not found in the XRD patterns. The discrepancy between the Scheil model and the experimental observations on phase formation in the alloy under investigation is likely due to non-equilibrium solidification conditions that are not fully accounted for in the thermodynamic simulation.

4.2. As-built microstructure

The distinct microstructural features found in the as-built Al-Fe-Ce alloy can be traced back to the specific solidification conditions of the PBF-LB/M process. Overall, the microstructure was refined due to high cooling rates typical of this fabrication process. The occasional presence of coarse Fe-rich dispersoids in proximity to the MPBs can be attributed to the lower cooling rate experienced by the MPBs in those regions compared to the center of the melt pool [50,51] coupled with the inherent thermal cycling caused by the layer-by-layer deposition [50,52]. This also explains the transition from a dendritic/coarse cellular microstructure to an extreme cellular one moving from the MPB to the center of the melt pool. Multiple intermetallic phases are dispersed in the coarse cellular network at the MPB. Based on previous observations done on other PBF-LB/Med Al-Fe alloys [17,19], it can be assumed that the relatively coarse Fe-rich intermetallics at the MPBs are the $Al_{13}Fe_4$ phase, as they are first to form according to the thermodynamic simulation. Conversely, Ce-rich intermetallics can be assumed to be $Al_{11}Ce_3$. In addition, the cellular network appears to be rich in both Ce and Fe as shown in Fig. 7. Finally, fine dispersoids are likely evenly distributed in

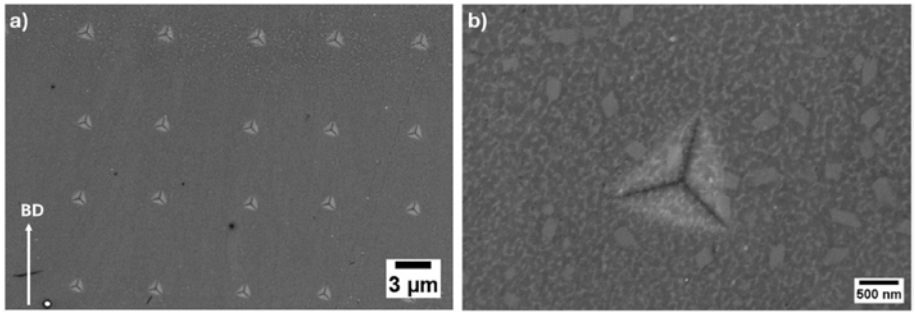

Fig. 9. (a) FESEM image of a portion of the nanoindentation matrix. (b) Magnification of a single nanoindentation imprint performed in the MPB region.

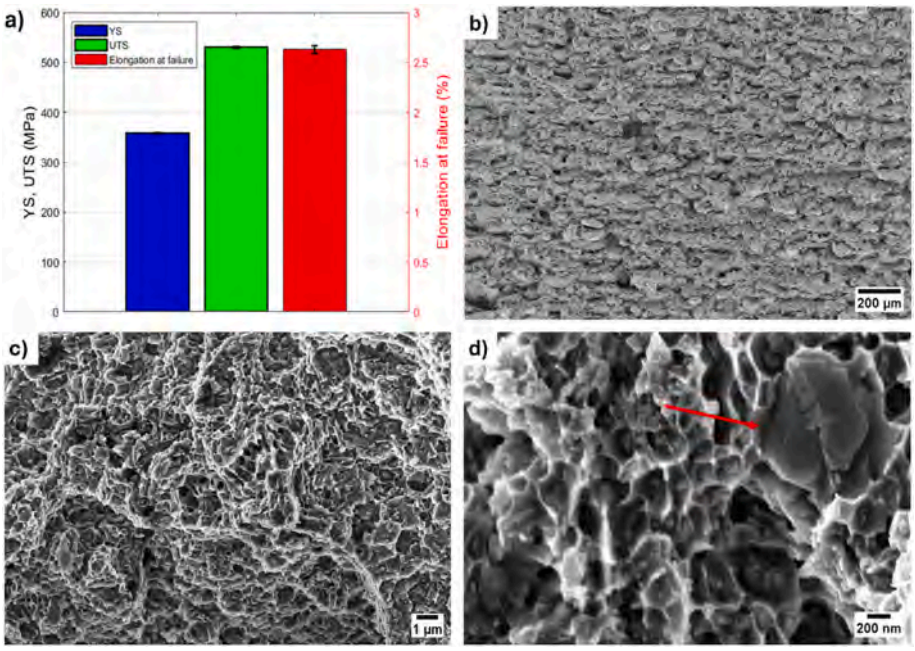

Fig. 10. (a) Main tensile properties of as-built Al-Fe-Ce alloy and (b)–(d) representative FESEM micrographs of a fracture surface for Al-Fe-Ce alloy after tensile test.

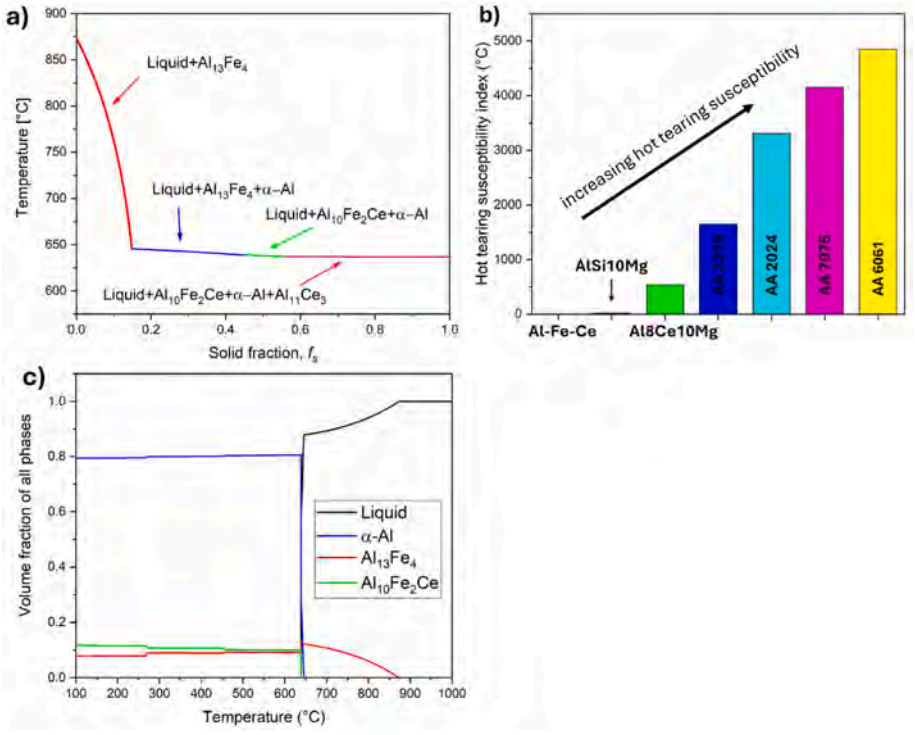

Fig. 11. (a) Scheil-Gulliver solidification curve for the Al-Fe-Ce alloy, (b) hot tearing susceptibility index for the Al-Fe-Ce alloy and for other Al alloys [11,49] and (c) phase fraction at equilibrium for the Al-Fe-Ce alloy.

the melt pool center, as suggested by Fig. 7e, where the extreme fine network is the result of the high cooling rate experienced during the PBF-LB/M process. As already mentioned, there is no evidence from XRD supporting the presence of the equilibrium $Al_{10}Fe_2Ce$ phase or metastable Al_8Fe_2Ce, even though their presence is suggested by both literature [15,32,34,35] and the Scheil-Gulliver model. This absence can be due to the solidification conditions that hindered their formation, or to a limited size that make it difficult to observe by FESEM or detected by XRD. Similar situation was observed by Belov et al. [53] studying casting Al-Ca-Fe alloys (a system similar to Al-Fe-Ce). They observed an incomplete peritectic transformation $L + Al_{13}Fe_4 \rightarrow \alpha\text{-Al} + Al_{10}CaFe_2$ with some $Al_{13}Fe_4$ left in a cast Al-6Ca-1Fe, even though it was expected its complete transformation. They explained this phenomenon by suggesting that the solidification conditions (cooling rate ~ 15 °C/s) were sufficient to partially inhibit the reaction. However, the precise intermetallic distribution in the Al-Fe-Ce alloy remains unclear and will be the matter of future research. The thermal history undergone by the material during fabrication can also explain the predominant coarse

columnar microstructure and the strong ⟨001⟩ texture parallel to the BD observed through EBSD analysis. In fact, this kind of microstructure is a direct consequence of the high cooling rates experienced during the PBF-LB/M process [2,54]. This was to some extent expected due to the lack of grain refiners such as Zr or Sc [54,55] in the alloy composition. These elements are typically added to Al alloys processed by AM since they are able to form coherent $L1_2$-type intermetallics [23,24,56] which can act as heterogenous nucleation sites, due to their favorable crystallographic structure and low lattice mismatch with the α-Al phase [54], allowing to produce a refined microstructure mainly composed of equiaxed grains in Al alloys [53]. In Al-Fe-Ce alloy, monoclinic $Al_{13}Fe_4$ [32] is the first phase to form, nevertheless, it does not meet the aforementioned criteria and thus cannot act as a heterogeneous nucleation site.

As shown by DSC, as-built Al-Fe-Ce alloy does not show any phase transformations up to 580 °C. This result was to some extent expected, as the traditional PM Al-Fe-Ce alloy is not heat-treatable [29]. Additionally, as mentioned in the Introduction, the alloy was designed as structural material for high temperature applications (up to approximately 350 °C), owing to the thermal stability of its intermetallic phases and the slow diffusion of Fe and Ce in the Al matrix [6]. Therefore, the only phenomenon that is expected to occur during holding at high temperature is the coarsening of the microstructure. However, at 580 °C, an exothermic reaction occurs. Although it could not be attributed to a specific transformation, this might be linked to the metastable Al_6Fe phase formed due to the far-from-equilibrium solidification condition induced by rapid solidification, as the corresponding peak disappeared during the second heating. The following peak, with an onset at 647 °C, could be linked to the dissolution of $Al_{11}Ce_3$ phase (Czerwinski [12] reported a melting temperature of roughly 645 °C for the eutectic Al-$Al_{11}Ce_3$) and the subsequent melting of the α-Al phase. At cooling, the first peak observed is the precipitation of the $Al_{13}Fe_4$ phase at 871 °C, which aligns well with the thermodynamic simulation. The subsequent peak, with the onset at 645 °C, is the overlapping of more phenomena, as indicated by its shape. As an equilibrium condition is approached during cooling, it can be assumed that the alloy follows the solidification path predicted by the equilibrium curve. Therefore, these phenomena can be associated with the solidification of α-Al, which is predicted to begin around 645 °C, followed by the precipitation of the $Al_{10}Fe_2Ce$ phase at approximately 639 °C. During the second heating, corresponding to the heating of the equilibrium structure of the Al-Fe-Ce alloy, the peak with onset at 639 °C is the sum of various phenomena, which is also suggested by its asymmetric shape. It can be speculated that these phenomena are the dissolution of the $Al_{10}Fe_2Ce$ followed by the melting of α-Al matrix. The second cooling ended up following the same solidification path of the first one, as both occur under near equilibrium conditions.

4.3. Mechanical properties

The mechanical tests performed on the as-built Al-Fe-Ce revealed that the alloy can achieve similar properties to traditional PM Al-Fe-Ce based systems [30,43] mainly due to the refinement of the microstructure given by the extreme cooling rate of the PBF-LB/M process. In addition, the alloy shows outstanding values of YS and UTS if compared to other PBF-LB/Med Al-Fe alloys [17,18,20,37], Al-Ce-Fe alloy [34] and AlSi10Mg [57], as shown in Fig. 12a. The mechanical properties are comparable to those of high strength Al-Fe-Cr alloy [25], Scalmalloy© [8], or Al-Fe-Sc-Zr [23], but providing the additional inherent advantage of eliminating potentially hazardous (e.g., Cr) and costly elements (such as Sc). On the other hand, the limited El of Al-Fe-Ce alloy compared to the other alloys (see Fig. 12b) may be attributed to high residual stress within the material in the as-built state (as observed in the KAM map) and relatively coarse Fe-rich intermetallics along the MPBs, as suggested by Wang et al. for Al-15Fe [19]. However, the high-volume fraction of intermetallic phases is also responsible for the exceptional hardness value of the Al-Fe-Ce alloy. The low standard deviation in nanohardness (particularly if compared to mechanical alloyed AlSi10Mg + 4 % Cu, where the hardest regions corresponded to Cu-rich areas due to a local de-mixing [58]), indicates that the microstructure of the Al-Fe-Ce alloy is generally homogenous, with most intermetallics refined as the result of rapid solidification.

5. Conclusions

This study investigated the processability of high-strength and heat-resistant Al-8Fe-4Ce (wt%) alloy by laser-based powder bed fusion for metals (PBF-LB/M), which was originally developed in the framework of traditional powder metallurgy. This alloy could exhibit a tendency to solid-state cracking due to this high-volume fraction of intermetallic phases and residual stress induced by the PBF-LB/M process.

The main findings are summarized hereafter:

- Crack-free samples with a relative density of 99.5 % were successfully produced by PBF-LB/M, using a high scanning speed (1200 mm/s) and a relative high value for hatching distance (0.16 mm), combined with a heated building platform (150 °C) and a 0°–90° cross ply scanning strategy.
- The refined microstructure of as-built samples, primarily composed of columnar grains, exhibits the presence of a high-volume fraction of intermetallic compounds dispersed in a cellular network rich in both Ce and Fe, with the relatively coarse ones predominately concentrated along the melt pool boundaries. However, the finest ones are homogeneously dispersed in all the melt pools. Residual stress originated during the PBF-LB/M process are primarily

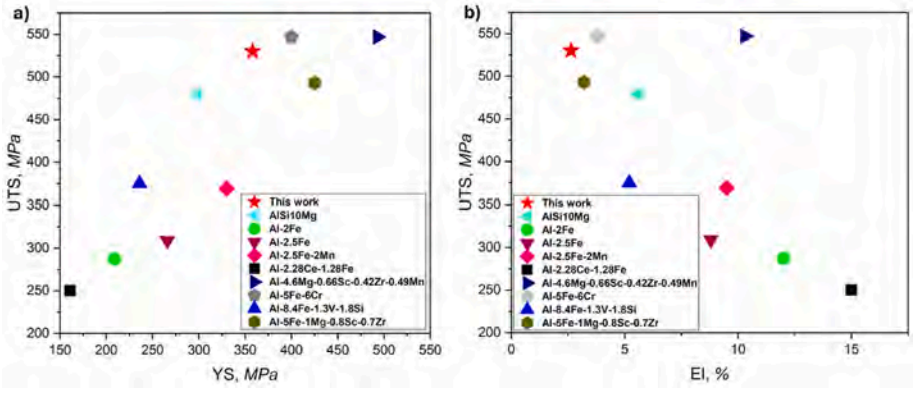

Fig. 12. (a) Comparison in yield strength and ultimate tensile strength for Al-Fe-Ce alloy and various Al alloys by PBF-LB/M. (b) Comparison in elongation at failure and ultimate tensile strength for Al-Fe-Ce alloy and various Al alloys.

concentrated along the melt pool boundaries regions and the low angle grain boundaries.

- XRD analysis identified different intermetallic phases, including $Al_{13}Fe_4$, $Al_{11}Ce_3$, and the metastable Al_6Fe phase. Although predicted by the Scheil–Gulliver solidification curve, the equilibrium $Al_{10}Fe_2Ce$ phase was not observed, probably due to the rapid solidification that hindered its formation.
- Thermal analyses confirmed the exceptional thermal stability of the alloy at temperatures beyond 200 °C, as the as-built alloy exhibits no phase transformations at temperatures up to 580 °C.
- Al-8Fe-4Ce possesses an average microhardness of 201 $HV_{0.5}$, an average nanohardness of 2.6 GPa and an ultimate tensile strength of 530 ± 1.6 MPa, comparable with the alloy processed by traditional powder metallurgy and PBF-LB/Med high strength Al alloys. In addition, its mechanical properties are also superior to those of other alloys based on Al-Fe system. The excellent mechanical properties are attributed to the high-volume fraction of very fine and homogeneously dispersed intermetallic phases.
- The interesting mechanical properties coupled with its thermal stability make PBF-LB/Med Al-8Fe-4Ce alloy a potential low cost alloy for structural applications at high temperatures, aligning it with the original purpose for which this alloy was developed.

CRediT authorship contribution statement

Nicolò Arcieri: Writing – original draft, Investigation, Formal analysis, Data curation, Conceptualization. **Silvia Marola:** Writing – review & editing, Investigation, Formal analysis, Data curation. **Marco Actis Grande:** Writing – review & editing, Supervision. **Diego Manfredi:** Writing – review & editing, Supervision, Funding acquisition, Conceptualization.

Declaration of competing interest

The authors declare that they have no known competing financial interests or personal relationships that could have appeared to influence the work reported in this paper.

Data availability

Data will be made available on request.

References

[1] T. DebRoy, H.L. Wei, J.S. Zuback, T. Mukherjee, J.W. Elmer, J.O. Milewski, A. M. Beese, A. Wilson-Heid, A. De, W. Zhang, Additive manufacturing of metallic components – process, structure and properties, Prog. Mater. Sci. 92 (2018) 112–224, https://doi.org/10.1016/j.pmatsci.2017.10.001.

[2] H.R. Kotadia, G. Gibbons, A. Das, P.D. Howes, A review of laser powder bed fusion additive manufacturing of aluminium alloys: microstructure and properties, Addit. Manuf. 46 (2021) 102155, https://doi.org/10.1016/j.addma.2021.102155.

[3] H. Groneberg, R. Horstkotte, M. Pruemmer, T. Bergs, F. Döpper, Concept for the reduction of non-value-adding operations in laser powder bed fusion (L-PBF), Proced. CIRP 107 (2022) 344–349, https://doi.org/10.1016/j.procir.2022.04.056.

[4] N.T. Aboulkhair, M. Simonelli, L. Parry, I. Ashcroft, C. Tuck, R. Hague, 3D printing of aluminium alloys: additive manufacturing of aluminium alloys using selective laser melting, Prog. Mater. Sci. 106 (2019) 100578, https://doi.org/10.1016/j.pmatsci.2019.100578.

[5] A. Plotkowski, K. Sisco, S. Bahl, A. Shyam, Y. Yang, L. Allard, P. Nandwana, A. M. Rossy, R.R. Dehoff, Microstructure and properties of a high temperature Al–Ce–Mn alloy produced by additive manufacturing, Acta Mater. 196 (2020) 595–608, https://doi.org/10.1016/j.actamat.2020.07.014.

[6] R.A. Michi, A. Plotkowski, A. Shyam, R.R. Dehoff, S.S. Babu, Towards high-temperature applications of aluminium alloys enabled by additive manufacturing, Int. Mater. Rev. 67 (2022) 298–345, https://doi.org/10.1080/09506608.2021.1951580.

[7] K. Schmidtke, F. Palm, A. Hawkins, C. Emmelmann, Process and mechanical properties: applicability of a scandium modified Al-alloy for laser additive manufacturing, Phys. Procedia 12 (2011) 369–374, https://doi.org/10.1016/j.phpro.2011.03.047.

[8] A.B. Spierings, K. Dawson, K. Kern, F. Palm, K. Wegener, SLM-processed Sc- and Zr-modified Al-Mg alloy: mechanical properties and microstructural effects of heat treatment, Mater. Sci. Eng., A 701 (2017) 264–273, https://doi.org/10.1016/j.msea.2017.06.089.

[9] S. Bahl, T. Wu, R.A. Michi, K. An, D. Yu, L.F. Allard, J.U. Rakhmonov, J. D. Poplawsky, C.M. Fancher, D.C. Dunand, A. Plotkowski, A. Shyam, An additively manufactured near-eutectic Al-Ce-Ni-Mn-Zr alloy with high creep resistance, Acta Mater. 268 (2024) 119787, https://doi.org/10.1016/j.actamat.2024.119787.

[10] H. Park, C.N. Ekaputra, D.C. Dunand, Microstructure and creep properties of Al-7Ce-3Ni-8Mg alloys fabricated by laser powder bed fusion of powder blends, Mater. Sci. Eng., A 926 (2025) 147968, https://doi.org/10.1016/j.msea.2025.147968.

[11] H. Hyer, A. Mehta, K. Graydon, N. Kljestan, M. Knezevic, D. Weiss, B. McWilliams, K. Cho, Y. Sohn, High strength aluminum-cerium alloy processed by laser powder bed fusion, Addit. Manuf. 52 (2022) 102657, https://doi.org/10.1016/j.addma.2022.102657.

[12] F. Czerwinski, Cerium in aluminum alloys, J. Mater. Sci. 55 (2020) 24–72, https://doi.org/10.1007/s10853-019-03892-z.

[13] Z.C. Sims, O.R. Rios, D. Weiss, P.E.A. Turchi, A. Perron, J.R.I. Lee, T.T. Li, J. A. Hammons, M. Bagge-Hansen, T.M. Willey, K. An, Y. Chen, A.H. King, S. K. McCall, High performance aluminum–cerium alloys for high-temperature applications, Mater. Horiz. 4 (2017) 1070–1078, https://doi.org/10.1039/C7MH00391A.

[14] D. Weiss, Improved high-temperature aluminum alloys containing cerium, J. Mater. Eng. Perform. 28 (2019) 1903–1908, https://doi.org/10.1007/s11665-019-3884-2.

[15] M.P. Moodispaw, E. Cinkilic, J. Miao, A.A. Luo, The beneficial effect of iron in aluminum-cerium-based cast alloys, Metall. Mater. Trans. 55 (2024) 1351–1362, https://doi.org/10.1007/s11661-024-07333-8.

[16] R.T. Nguyen, D.D. Imholte, O.R. Rios, D. Weiss, Z. Sims, E. Stromme, S.K. McCall, Anticipating impacts of introducing aluminum-cerium alloys into the United States automotive market, Resour. Conserv. Recycl. 144 (2019) 340–349, https://doi.org/10.1016/j.resconrec.2019.02.009.

[17] Y. Wu, T. Zhang, C. Chen, S.R.E. Hosseini, X. Zhang, K. Zhou, Microstructure and mechanical property evolution of additive manufactured eutectic Al-2Fe alloy during solidification and aging, J. Alloys Compd. 897 (2022) 163243, https://doi.org/10.1016/j.jallcom.2021.163243.

[18] X. Qi, N. Takata, A. Suzuki, M. Kobashi, M. Kato, Change in microstructural characteristics of laser powder bed fused Al–Fe binary alloy at elevated temperature, J. Mater. Sci. Technol. 97 (2022) 38–53, https://doi.org/10.1016/j.jmst.2021.04.038.

[19] W. Wang, N. Takata, A. Suzuki, M. Kobashi, M. Kato, Formation of multiple intermetallic phases in a hypereutectic Al–Fe binary alloy additively manufactured by laser powder bed fusion, Intermetallics 125 (2020) 106892, https://doi.org/10.1016/j.intermet.2020.106892.

[20] W. Wang, N. Takata, A. Suzuki, M. Kobashi, M. Kato, Design of Al–Fe–Mn alloy for both high-temperature strength and sufficient processability of laser powder bed fusion, Addit. Manuf. 68 (2023) 103524, https://doi.org/10.1016/j.addma.2023.103524.

[21] Y. Cheng, T. Miyawaki, W. Wang, N. Takata, A. Suzuki, M. Kobashi, M. Kato, Laser-beam powder bed fusion of Al–Fe–Cu alloy to achieve high strength and thermal conductivity, Addit. Manuf. Letters 8 (2024) 100191, https://doi.org/10.1016/j.addlet.2023.100191.

[22] Z. Sun, M. Roscher, M.C. Paolantonio, V. Soh, C. Liu, S.-P. Tsai, C.K. Ng, C.C. Tan, P. Wang, E.A. Jägle, Additive manufacturing of sustainable and heat-resistant Al-Fe-Mo-Si-Zr alloys, J. Alloys Compd. 1010 (2025) 177118, https://doi.org/10.1016/j.jallcom.2024.177118.

[23] Y. Wang, R. Li, T. Yuan, L. Zou, M. Wang, H. Yang, Microstructure and mechanical properties of Al-Fe-Sc-Zr alloy additively manufactured by selective laser melting, Mater. Char. 180 (2021) 111397, https://doi.org/10.1016/j.matchar.2021.111397.

[24] Y. Wang, R. Li, J. Li, L. Zou, T. Yuan, J. Li, X. Liu, D. Lai, Toward the superior high-temperature strength of Al-5Fe alloy for powder bed fusion-laser beam: stabilizing Al6Fe nanoprecipitate by Sc and Zr elements, Mater. Sci. Eng., A 897 (2024) 146351, https://doi.org/10.1016/j.msea.2024.146351.

[25] M.T. Pérez-Prado, A. Martin, D.F. Shi, S. Milenkovic, C.M. Cepeda-Jiménez, An Al-5Fe-6Cr alloy with outstanding high temperature mechanical behavior by laser powder bed fusion, Addit. Manuf. 55 (2022) 102828, https://doi.org/10.1016/j.addma.2022.102828.

[26] X. Qi, N. Takata, A. Suzuki, M. Kobashi, M. Kato, Laser powder bed fusion of a near-eutectic Al–Fe binary alloy: processing and microstructure, Addit. Manuf. 35 (2020) 101308, https://doi.org/10.1016/j.addma.2020.101308.

[27] W. Mohammed, X. Chen, D. Ponge, D. Raabe, Thermodynamics-guided design of sustainable secondary Al-Si alloys for enhanced Fe-impurity tolerance and optimized Mn doping, Acta Mater. 289 (2025) 120932, https://doi.org/10.1016/j.actamat.2025.120932.

[28] D. Raabe, D. Ponge, P.J. Uggowitzer, M. Roscher, M. Paolantonio, C. Liu, H. Antrekowitsch, E. Kozeschnik, D. Seidmann, B. Gault, F. De Geuser, A. Deschamps, C. Hutchinson, C. Liu, Z. Li, P. Prangnell, J. Robson, P. Shanthraj, S. Vakili, C. Sinclair, L. Bourgeois, S. Pogatscher, Making sustainable aluminum by recycling scrap: the science of "dirty" alloys, Prog. Mater. Sci. 128 (2022) 100947, https://doi.org/10.1016/j.pmatsci.2022.100947.

[29] S. Langenbeck, W. Griffith, G. Hildeman, J. Simon, Development of dispersion-strengthened aluminum alloys, in: Rapidly Solidified Powder Aluminum Alloys, ASTM International100 Barr Harbor Drive, PO Box C700, West Conshohocken, PA, 1986, pp. 410–422, https://doi.org/10.1520/STP33042S, 19428-2959.

[30] W.M. Griffith, R.E. Sanders Jr., G.J. Hildeman, Elevated temperature aluminum alloys for aerospace applications, in: High Strength Powder Metallurgy Aluminum Alloys, The Metallurgical Society of AIME, Warrendale, PA, 1982, pp. 209–224.
[31] Y.-W. Kim, Processing/microstructure/properties of Al-Fe-Ce powder alloys, in: Dispersion Strengthened Aluminum Alloys, TMS, Warrendale, PA, 1988, pp. 157–180.
[32] M.L. Öveçoglu, C. Suryanarayana, W.D. Nix, Identification of precipitate phases in a mechanically alloyed rapidly solidified Al-Fe-Ce alloy, Metall. Mater. Trans. 27 (1996) 1033–1041, https://doi.org/10.1007/BF02649771.
[33] U. Prakash, T. Raghu, A.A. Gokhale, S.V. Kamat, Microstructure and mechanical properties of RSP/M Al-Fe-V-Si and Al-Fe-Ce alloys, J. Mater. Sci. 34 (1999) 5061–5065, https://doi.org/10.1023/A:1004700830936.
[34] S.V. Chernyshikhin, E.L. Dzidziguri, L.V. Fedorenko, A.A. Gromov, K.B. Larionov, M.V. Lyange, N.A. Kharitonova, E.A. Naumova, D.Yu Ozherelkov, I.A. Pelevin, S. O. Rogachev, Structure and mechanical properties of al–ce–fe alloy synthesized by LPBF method, Met. Mater. Int. 30 (2024) 3184–3201, https://doi.org/10.1007/s12540-024-01698-6.
[35] H.S. Park, C.N. Ekaputra, D.C. Dunand, Effect of Fe additions on microstructure and mechanical properties in near-eutectic Al–Ce alloys, Mater. Sci. Eng., A 882 (2023) 145409, https://doi.org/10.1016/j.msea.2023.145409.
[36] S.-B. Sun, L.-J. Zheng, J.-H. Liu, H. Zhang, Microstructure, cracking behavior and control of Al–Fe–V–Si alloy produced by selective laser melting, Rare Met. 42 (2023) 1353–1362, https://doi.org/10.1007/s12598-016-0846-9.
[37] S. Wei, S. Huang, S.J. Ng, L. Zhang, Y. Zeng, P. Wang, U. Ramamurty, Suppressing cold cracking in laser powder bed fused Al-Fe-V-Si alloy using top-hat laser profile, Mater. Sci. Eng., A 924 (2025) 147858, https://doi.org/10.1016/j.msea.2025.147858.
[38] W.C. Oliver, G.M. Pharr, An improved technique for determining hardness and elastic modulus using load and displacement sensing indentation experiments, J. Mater. Res. 7 (1992) 1564–1583, https://doi.org/10.1557/JMR.1992.1564.
[39] A. Mehta, T. Huynh, N. Kljestan, K. Graydon, A. Mahmud, M. Knezevic, B. McWilliams, K. Cho, Y. Sohn, Additive manufacturing of Al18Co30Cr10Fe10Ni32 high entropy alloy by gas atomization and laser powder bed fusion, Mater. Lett. 350 (2023) 134942, https://doi.org/10.1016/j.matlet.2023.134942.
[40] A.J. Schwartz, M. Kumar, B.L. Adams, D.P. Field (Eds.), Electron Backscatter Diffraction in Materials Science, Springer US, Boston, MA, 2009, https://doi.org/10.1007/978-0-387-88136-2.
[41] C. Phutela, F. Bosio, P. Li, N.T. Aboulkhair, Correlating the microstructure and hardness of AlSi10Mg powder with additively-manufactured parts upon in-situ heat-treatments in laser beam powder bed fusion, Addit. Manuf. Letters 7 (2023) 100168, https://doi.org/10.1016/j.addlet.2023.100168.
[42] S. Marola, D. Gianoglio, F. Bosio, A. Aversa, M. Lorusso, D. Manfredi, M. Lombardi, L. Battezzati, Alloying AlSi10Mg and Cu powders in laser Single Scan Tracks, melt spinning, and Laser Powder Bed Fusion, J. Alloys Compd. 821 (2020) 153538, https://doi.org/10.1016/j.jallcom.2019.153538.
[43] U. Prakash, T. Raghu, S.V. Kamat, A.A. Gokhale, The effect of Mg addition on microstructure and tensile and stress rupture properties of a P/M Al-Fe-Ce alloy, Scr. Mater. 39 (1998) 867–872, https://doi.org/10.1016/S1359-6462(98)00258-9.
[44] J. Fu, H. Li, X. Song, M.W. Fu, Multi-scale defects in powder-based additively manufactured metals and alloys, J. Mater. Sci. Technol. 122 (2022) 165–199, https://doi.org/10.1016/j.jmst.2022.02.015.
[45] A. Fardan, A. Fazi, R.L. Peng, T. Mishurova, M. Thuvander, G. Bruno, H. Brodin, E. Hryha, Fine-tuning melt pools and microstructures: taming cracks in powder bed fusion—laser beam of a non-weldable Ni-base superalloy, Materialia 34 (2024) 102059, https://doi.org/10.1016/j.mtla.2024.102059.
[46] N. Nadammal, T. Mishurova, T. Fritsch, I. Serrano-Munoz, A. Kromm, C. Haberland, P.D. Portella, G. Bruno, Critical role of scan strategies on the development of microstructure, texture, and residual stresses during laser powder bed fusion additive manufacturing, Addit. Manuf. 38 (2021) 101792, https://doi.org/10.1016/j.addma.2020.101792.
[47] S. Kou, A criterion for cracking during solidification, Acta Mater. 88 (2015) 366–374, https://doi.org/10.1016/j.actamat.2015.01.034.
[48] M.J. Benoit, S.M. Zhu, T.B. Abbott, M.A. Easton, Evaluation of the effect of rare Earth alloying additions on the hot tearing susceptibility of aluminum alloy 7150 during rapid solidification, Metall. Mater. Trans. 51 (2020) 5213–5227, https://doi.org/10.1007/s11661-020-05930-x.
[49] T. Soysal, S. Kou, A simple test for assessing solidification cracking susceptibility and checking validity of susceptibility prediction, Acta Mater. 143 (2018) 181–197, https://doi.org/10.1016/j.actamat.2017.09.065.
[50] P. Van Cauwenbergh, V. Samaee, L. Thijs, J. Nejezchlebová, P. Sedlák, A. Iveković, D. Schryvers, B. Van Hooreweder, K. Vanmeensel, Unravelling the multi-scale structure–property relationship of laser powder bed fusion processed and heat-treated AlSi10Mg, Sci. Rep. 11 (2021) 6423, https://doi.org/10.1038/s41598-021-85047-2.
[51] A. Pandey, S. Choudhary, V. Gaur, A numerical study on microstructural features evolved across the melt pool in additively manufactured IN718 alloy, Mater. Sci. Eng., A 868 (2023) 144763, https://doi.org/10.1016/j.msea.2023.144763.
[52] H. Hu, X. Ding, L. Wang, Numerical analysis of heat transfer during multi-layer selective laser melting of AlSi10Mg, Optik 127 (2016) 8883–8891, https://doi.org/10.1016/j.ijleo.2016.06.115.
[53] N.A. Belov, T.K. Akoyan, E.A. Naumova, V.V. Doroshenko, T.A. Sviridova, N. O. Korotkova, Formation and characterization of Al10CaFe2 compound in Al−Ca−Fe alloys, Trans. Nonferrous Metals Soc. China 34 (2024) 361–377, https://doi.org/10.1016/S1003-6326(23)66404-0.
[54] K.V. Yang, Y. Shi, F. Palm, X. Wu, P. Rometsch, Columnar to equiaxed transition in Al-Mg(-Sc)-Zr alloys produced by selective laser melting, Scr. Mater. 145 (2018) 113–117, https://doi.org/10.1016/j.scriptamat.2017.10.021.
[55] D. Zhang, A. Prasad, M.J. Bermingham, C.J. Todaro, M.J. Benoit, M.N. Patel, D. Qiu, D.H. StJohn, M. Qian, M.A. Easton, Grain refinement of alloys in fusion-based additive manufacturing processes, Metall. Mater. Trans. 51 (2020) 4341–4359, https://doi.org/10.1007/s11661-020-05880-4.
[56] S. Bahl, K. Sisco, Y. Yang, F. Theska, S. Primig, L.F. Allard, R.A. Michi, C. Fancher, B. Stump, R. Dehoff, A. Shyam, A. Plotkowski, Al-Cu-Ce(-Zr) alloys with an exceptional combination of additive processability and mechanical properties, Addit. Manuf. 48 (2021) 102404, https://doi.org/10.1016/j.addma.2021.102404.
[57] I. Rosenthal, R. Shneck, A. Stern, Heat treatment effect on the mechanical properties and fracture mechanism in AlSi10Mg fabricated by additive manufacturing selective laser melting process, Mater. Sci. Eng., A 729 (2018) 310–322, https://doi.org/10.1016/j.msea.2018.05.074.
[58] F. Bosio, D. Manfredi, M. Lombardi, Homogenization of an Al alloy processed by laser powder bed fusion in-situ alloying, J. Alloys Compd. 904 (2022), https://doi.org/10.1016/j.jallcom.2022.164079.